Research Article

Nano Research
2022, 15(8): 7220–7226

ISSN 1998-0124 CN 11-5974/O4
https://doi.org/10.1007/s12274-022-4398-z

Novel metastable Bi:Co and Bi:Fe alloys nanodots@carbon as anodes for high rate K-ion batteries

Zhongqiu Tong[1,2,3], Tianxing Kang[2,3], Yan Wu[2,3], Fan Zhang[4], Yongbing Tang[4] (✉), and Chun-Sing Lee[2,3] (✉)

[1] *Faculty of Metallurgical and Energy Engineering, Kunming University of Science and Technology, Kunming 650093, China*
[2] *Department of Chemistry, City University of Hong Kong, Hong Kong 999077, China*
[3] *Center of Super-Diamond and Advanced Films (COSDAF), City University of Hong Kong, Hong Kong 999077, China*
[4] *Shenzhen Institutes of Advanced Technology, Chinese Academy of Sciences, Shenzhen 518055, China*

Received: 17 March 2022 / **Revised:** 31 March 2022 / **Accepted:** 4 April 2022

ABSTRACT

Bi is a promising anode material for potassium-ion batteries (PIBs) due to its high theoretical capacity. However, severe pulverization upon cycling limits its practical applications. In this work, we propose a new approach of using metastable alloys with Bi elements. Metastable Bi:Co and Bi:Fe alloys nanodots@carbon anode materials (Bi:Co and Bi:Fe@C) are synthesized for the first time via simple annealing of their metal-organic frameworks (MOF) precursors. These prepared materials are demonstrated as ideal hosts for high-rate K-ion storage. $Bi_{0.85}Co_{0.15}$@C and $Bi_{0.83}Fe_{0.17}$@C electrodes respectively deliver superior 178 and 253 mAh·g^{-1} at 20 A·g^{-1}, as well as stable cycling performance at 2 A·g^{-1}. *Ex situ* scanning electron microscopy (SEM), X-ray photoelectron spectroscopy (XPS), X-ray diffraction (XRD), and transmission electron microscopy (TEM) studies on Bi:Co@C indicate that the elemental Co separates out during the initial potassiation and stands during the following discharge/charge cycles. *In situ* formed Co precipitates can act as (1) "conductive binders" as well as (2) "separators" to prevent the severe aggregation of adjacent active elemental Bi nanoparticles and (3) accelerate the potassiation/de-potassiation kinetics in elemental Bi precipitates after initial discharge/charge cycles. This work could inspire the development of metal-type anodes.

KEYWORDS

metastable alloys, metal anode, potassium-ion battery, metal-organic frameworks (MOF)-derived materials

1 Introduction

Potassium-ion batteries (PIBs) are considered as a promising alternative to lithium-ion batteries (LIBs) owing to the abundant potassium resources, low costs, and fast ionic conductivity in electrolyte [1–3]. To achieve full PIBs with good stability, fabrication of anode materials that can store potassium over a low potential range (around 0.3 V) to avoid dendrite formation is an important key [4]. While metals in groups 13–15 of the periodic table do meet these requirements [5, 6], their severe pulverization often leads to loss of electrical contact during K-ion uptake/extraction [6–8]. This problem has been addressed by using intermetallic compounds of these metallic elements as anodes [9, 10]. It was observed that the intermetallic compounds would be decomposed into their constituting metal upon discharging. The two metallic phases can better accommodate the volume changes and/or form better electrical conducting paths [11, 12]. Indeed, improved cycling stability was observed in intermetallic anodes. However, due to the strong intermetallic bonds, the separated metals re-alloy and form intermetallic compounds again upon charging [12–15]. For this reason, the issue of pulverization in long-term tests is not fully addressed.

Based on these pioneering works, it is natural to ask a question that, if we can stop the re-alloying process in the intermetallics upon charging, will the issue of pulverization be much better addressed? Here, we attempt to answer this question by preparing metastable alloys anodes which can naturally stop the re-alloying process upon charging because of their metastable nature. The main challenge is that due to the metastable nature, it is difficult to obtain such nanoscaled alloy materials [16–18]. In fact, up till now, there is no report on metastable alloy anodes for PIBs.

In this work, we prepare metastable Bi:Co and Bi:Fe alloy anodes for the first time from their metal-organic frameworks (MOFs) precursors. In the MOF's microenvironment, the two types of metal ions are distributed homogenously. Upon annealing decomposition treatment, they form metastable alloy, instead of elemental metallic, nanoparticles. These alloy nanodots are embedded in amorphous carbon stemming from the organic constituents in the MOFs. To demonstrate the electrochemical superiority of the metastable alloys, Bi is chosen as the active alloying element due to its high theoretical capacity [19–23]. Similar to the reported stable intermetallic anodes, the present metastable alloy anodes will also be decomposed into their constituting metal elements upon potassiation. However, due to their metastable nature, the alloys cannot be reformed upon de-potassiation. *Ex situ* studies on Bi:Co@C show that the precipitated elemental active (Bi) and inactive (Co) nanoparticles are of 10–20 nm diameter and distribute uniformly. The electrochemically inactive Co nanodots can act as (1) "conductive binders" as well as (2) "separators" to prevent the severe aggregation of adjacent Bi precipitates and (3) accelerate the

Address correspondence to Yongbing Tang, tangyb@siat.ac.cn; Chun-Sing Lee, apcslee@cityu.edu.hk

potassiation/de-potassiation kinetics in active Bi precipitates during the discharge/charge cycles. With these effects, the metastable alloy anodes deliver high rate K-ion storage under high current density of 20 $A \cdot g^{-1}$ (178 and 253 $mAh \cdot g^{-1}$ for the $Bi_{0.85}Co_{0.15}$@C and $Bi_{0.83}Fe_{0.17}$@C electrodes respectively) with stable cycling performance at 2 $A \cdot g^{-1}$. The capacity and cycling stability of the $Bi_{0.83}Fe_{0.17}$@C anode are among the best comparing to recently reported PIB anode materials.

2 Results and discussion

The anode materials with metastable Bi:Co and Bi:Fe alloys nanodots embedded in amorphous carbon are prepared by annealing MOF precursors (Fig. 1(a)). Bi-Co and Bi-Fe MOFs particles were first prepared via a solvothermal process with the corresponding metal cations and trimesic acid (H_3BTC) (Fig. S1 in the Electronic Supplementary Material (ESM)). After annealing the MOFs in Ar/H_2 atmosphere at 600 °C, Bi:Co@C and Bi:Fe@C ($Bi_{0.83}Fe_{0.17}$@C) powders were obtained. As shown by their X-ray diffraction (XRD) patterns (Fig. 1(b)), besides the $Bi_{0.73}Co_{0.27}$@C and $Bi_{0.64}Co_{0.36}$@C demonstrating some weak signals from phase impurities, Bi:Co@C materials show similar crystalline phase to rhombohedral Bi (PDF no. 44-1246) with small peak shifts of ~ 0.4° to 0.5°. The shift of diffraction Bi peaks implies the inactive Co element might be alloyed with the active Bi element. Scanning electron microscopy (SEM) analysis shows that the Bi:Co@C samples are micrometer sized particles (Fig. 1(c) and Figs. S2(a)–S2(d) in the ESM). D and G Raman bands of samples indicate the presence of carbon (Fig. S2(e) in the ESM) [24].

Transmission electron microscopy (TEM) measurement was employed to analyze microstructures of the Bi:Co@C particles. It is observed that the synthesized sample composes of loosely packed nanodots embedded in carbon (Figs. 1(d) and 1(e)). High magnification TEM images show that the diameter of sphere-like nanodots is below ~ 20 nm (Fig. S3(a) in the ESM) and the coated carbon is of amorphous nature (Fig. S3(b) in the ESM). Elemental mapping results (Figs. S3(c)–S3(e) in the ESM) confirm the nanodots are composed of Bi and Co meanwhile the nanodots are uniformly distributed in the carbon matrix. To get more information about the nanodots, high-resolution TEM (HRTEM) studies were conducted. As shown in Fig. 1(f), a metal particle shows lattice fringe intervals of 0.339 and 0.201 nm with angle of 119.9°. While, these values do not match with those of crystalline cobalt, they are similar to the lattice spacing of (012) and (006) planes (corresponding to 0.328 and 0.197 nm, respectively) with an angle of 122.7° of rhombohedral Bi. Another metal particle demonstrates lattice fringe intervals of 0.208 and 0.231 nm with angle of 118.5° (Fig. 1(g)). These values are also similar to the crystalline parameters of rhombohedral Bi (intervals of 0.202 and 0.227 for (015) and (110) planes, respectively, angle of 116.4°). These HRTEM results are consistent with the XRD patterns. During the annealing process, cobalt with small atomic radius can dissolved into the lattice of rhombohedral Bi particles to form metastable Bi:Co alloy particles. It is believed that the formation of alloy instead of elemental metallic nanodots is due to the microenvironment in the MOFs in which the two types of metal cations are homogenously distributed [16]. Physical examinations indicate that the Bi-Fe MOF-derived material also demonstrate metastable Bi:Fe alloy nanodots@carbon structure ($Bi_{0.83}Fe_{0.17}$@C, Fig. S4 in the ESM). Diameter of the Bi:Fe alloy nanodots is also below ~ 20 nm. The Bi MOF-derived material shows Bi nanodots@carbon structure (Bi@C, Fig. S5 in the ESM).

Electrochemical performances of the Bi:Co@C and the Bi:Fe@C materials were evaluated in 1 M KPF_6/dimethoxyethane (DME) solutions over a potential window of 0.1–1.5 V in 2032 coin cells with K foils as the counter electrodes. After activation of the initial discharge process, the Bi:Co@C electrodes demonstrate a typical Bi-based K-ion uptake/release profiles (Figs. S6(a) and S6(b) in the

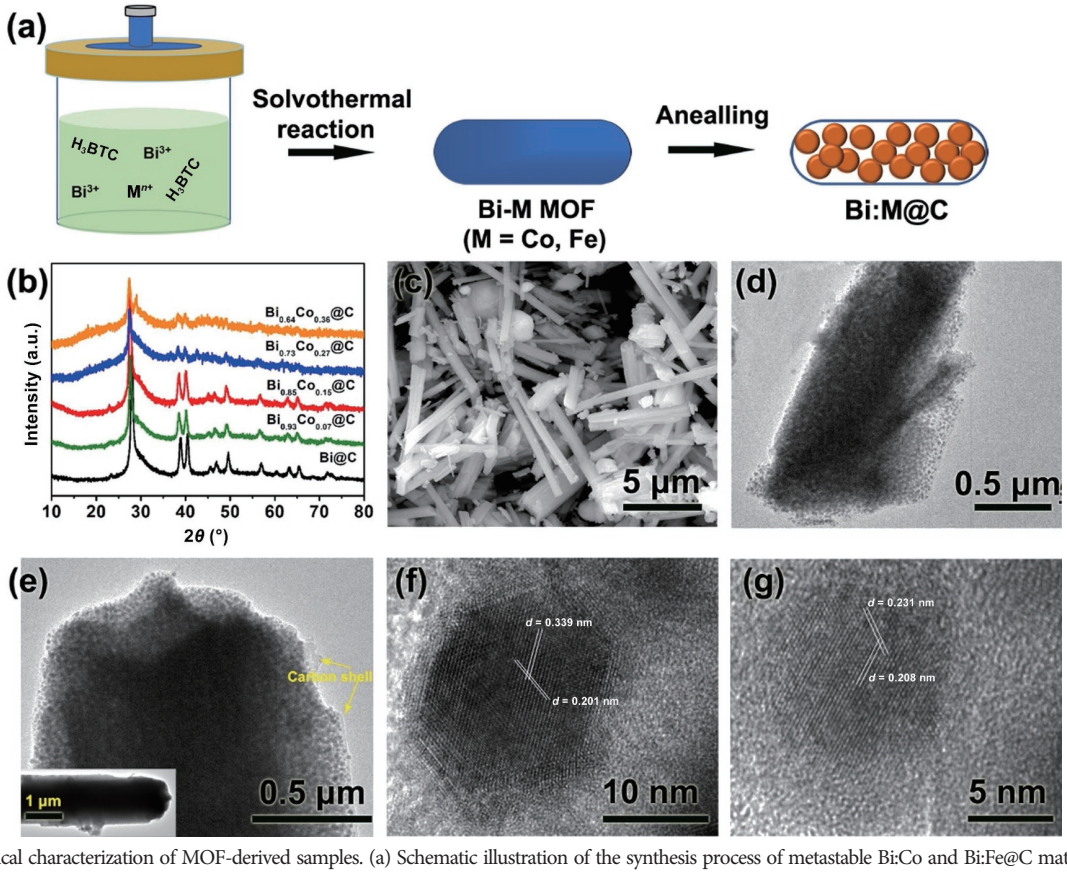

Figure 1 Physical characterization of MOF-derived samples. (a) Schematic illustration of the synthesis process of metastable Bi:Co and Bi:Fe@C materials. (b) XRD patterns of Bi:Co@C particles. SEM (c), TEM (d) and (e), and HRTEM (f) and (g) images of $Bi_{0.85}Co_{0.15}$@C particles.

ESM) [19–23], implying the main energy storage might be mainly contributed by elemental Bi nanodots precipitated from the Bi:Co alloys. Charge/discharge tests under different current densities show superior specific capacity and rate capability for the Bi:Co@C electrodes. As demonstrated in Fig. 2(a), along with the increase of Co molar ratio, rate capability of the Bi:Co@C electrodes first increases and then decreases with the best performance in the $Bi_{0.85}Co_{0.15}$@C electrode. The $Bi_{0.85}Co_{0.15}$@C electrode delivers a specific discharge capacity of 364 and 258 mAh·g^{-1} at 0.2 and 5 A·g^{-1}, which is considerably higher than those of the Bi@C electrode (301 and 217 mAh·g^{-1}, respectively). Notably, the $Bi_{0.85}Co_{0.15}$@C and $Bi_{0.73}Co_{0.27}$@C electrodes respectively demonstrate high capacity of 178 and 152 mAh·g^{-1} at a high current density of 20 A·g^{-1}, in contrast to the much lower capacity of 77 mAh·g^{-1} for the Bi@C electrode. The $Bi_{0.85}Co_{0.15}$@C electrodes with areal mass loadings between 0.7 to 11.2 mg·cm^{-2} exhibit a similar rate capability, confirming the electrochemical advantages of the Bi:Co@C materials (Fig. 2(b)).

The $Bi_{0.83}Fe_{0.17}$@C electrode delivers superior rate capability of 354, 279, and 253 mAh·g^{-1} at 0.2, 5, and 20 A·g^{-1}, respectively (Fig. 2(c) and Figs. S7(a) and S7(b) in the ESM). Capacity retention of the $Bi_{0.83}Fe_{0.17}$@C and the $Bi_{0.85}Co_{0.15}$@C anodes under such high current densities shows performance comparable to state-of-the-art metallic, sulfide, carbon, and oxide anodes (Fig. 2(d)) [20, 22, 25–34], indicating their potential for practical PIB applications. The Bi:Co@C and the Bi:Fe@C materials also demonstrate significantly enhanced cycling stability. As shown in Fig. 2(e) and Figs. S7(c) in the ESM, they demonstrate stable cycling performance for approximately 1,000 cycles at a high current density of 2 A·g^{-1}. The maintained discharge capacities of the $Bi_{0.85}Co_{0.15}$@C and the $Bi_{0.83}Fe_{0.17}$@C electrodes are 218 and 279 mAh·g^{-1} after 1,000 and 975 cycles, respectively. The mass loading-independent cycling performance of $Bi_{0.85}Co_{0.15}$@C further confirms the electrochemical advantages of the metastable alloy@C materials prepared by the proposed approach (Fig. S6(c) in the ESM).

K-ion uptake mechanism of the Bi:Co@C electrodes was first investigated through *ex situ* XRD studies (Fig. 3(a)). $Bi_{0.85}Co_{0.15}$@C material (mixed with 5 wt.% of super P and 5 wt.% of polyvinylidene fluoride) was casted on a titanium foil. As demonstrated in Figs. 3(b) and 3(c), accompanying with the increase of capacity, the typical Bi-K alloying-based storage characteristic becomes obvious during the initial four cycles. These phenomena indicate that there is an electrochemical activation process occurring in the prepared metastable Bi:Co nanodots. As shown by *ex situ* XRD patterns (Fig. 3(a)), upon initial potassiation to 0.1 V, XRD signals of the Bi:Co alloy decrease, meanwhile the signals assigned to K_3Bi and elemental fcc Co precipitate increase. The fcc Co XRD peak does not disappear when electrode is charged to 1.5 V, indicating the prepared Bi:Co alloy does not recover. During the following discharge/charge cycles, along with the reversible phase changes between Bi and K_3Bi, fcc Co always exists and signals of elemental hcp Co emerge after 10 discharge/charge cycles. In addition, as shown in *ex situ* X-ray photoelectron spectroscopy (XPS) results, during the 4th discharge/charge cycle, no oxidized Bi signals are observed (Fig. 3(d)), meanwhile the atomic ratio of Co^0:Co^{2+} is high and stable (Fig. 3(e)). These phenomena confirm that K-ion storage is almost entirely from the elemental Bi generated from decomposition of the metastable Bi:Co alloys.

TEM examination was further employed to determine the phase compositions of the Bi:Co@C sample after K-ion

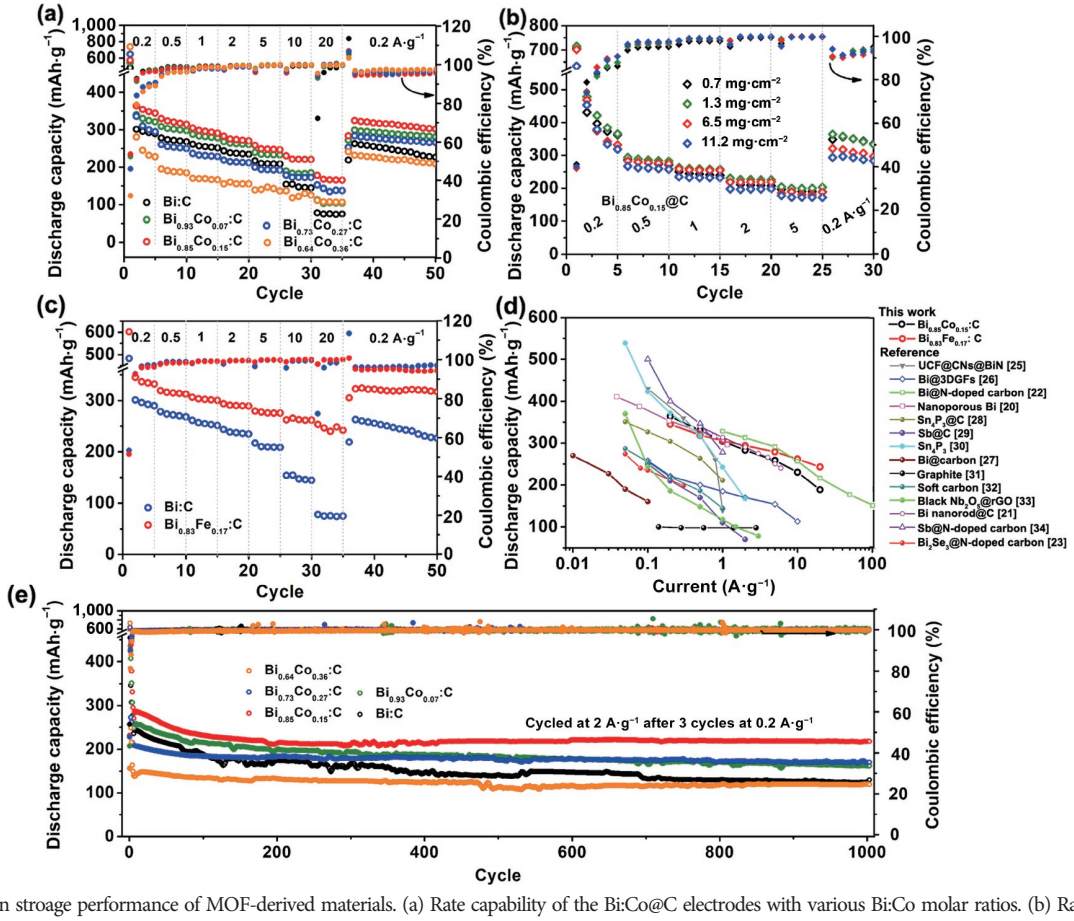

Figure 2 K-ion stroage performance of MOF-derived materials. (a) Rate capability of the Bi:Co@C electrodes with various Bi:Co molar ratios. (b) Rate capability of the $Bi_{0.73}Co_{0.27}$@C electrodes with different mass loadings. (c) Rate capability of the $Bi_{0.83}Fe_{0.17}$@C electrode. (d) Comparison of the rate capability with the reported anode materials for PIBs. (e) Cycling performance of the Bi:Co@C electrodes with the various Bi:Co molar ratios.

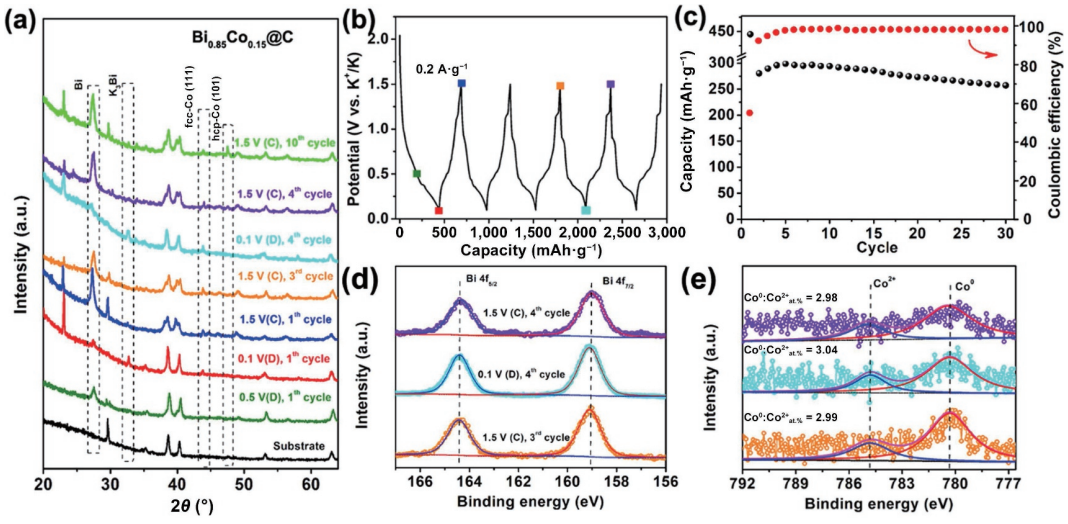

Figure 3 Determination of K-ion storage mechanism of MOF-derived materials. (a) *Ex situ* XRD patterns of the $Bi_{0.85}Co_{0.15}$@C electrodes recorded during discharge/charge processes. "D" and "C" are discharge and charge, respectively. Discharge/charge curves (b) and cycling performance (c) of the $Bi_{0.85}Co_{0.15}$@C electrodes at 0.2 A·g^{-1}. *Ex situ* high-resolution Bi 4f (d) and Co 2p (e) XPS spectra of the $Bi_{0.85}Co_{0.15}$@C electrodes during 4th discharge/charge process.

uptake/release kinetics becomes stable. Figure S8(a) in the ESM shows TEM image of a $Bi_{0.85}Co_{0.15}$@C sample at its fully charged (i.e., de-potassiated) state after 3 discharge/charge cycles. As shown in the HRTEM image (Fig. S8(b) in the ESM), it finds that the carbon shell demonstrates high flexibility to accommodate the volume expansion/shrink from the Bi potassiation/de-potassiation. Additionally, it can be seen that the cycled Bi:Co@C material demonstrates a porous characteristic, similar to the freshly prepared material (i.e., before cycling). A HRTEM image of the charged sample is shown in Fig. S8(c) in the ESM, demonstrating that the precipitated elemental Bi nanoparticles are separated by precipitated Co nanoparticles. Furthermore, as indicated by TEM and HRTEM images of the fully discharge sample (Figs. S8(d) and S8(e) in the ESM), it is found that the K-ion uptake in Bi nanoparticles does not change the porous morphology nor the intimate contact between two types of precipitated nanoparticles, indicating the microstructure stability of samples. The uniform C, Bi, and Co elemental distributions of fully charged $Bi_{0.85}Co_{0.15}$@C sample clearly demonstrate the intimate interactions between precipitated Bi and Co nanoparticles (Fig. S8(f) in the ESM).

In contrast, in Bi@C material, repeated volume expansion/shrink from potassiation/de-potassiation gives rise to "dead" Bi and K_3Bi with electrochemical inactivity after initial several cycles, as shown in *ex situ* XRD patterns (Fig. S9(a) in the ESM). Furthermore, the repeated volume expansion/shrink also leads to the severe aggregation of adjacent Bi particles, generating large particle with long K-ion diffusion distance (Figs. S9(b)–S9(e) in the ESM). Combining these comparison analysis results of Bi:Co@C and Bi@C samples, it concludes the precipitated Co nanoparticles can act as "separators" to prevent the adjacent precipitated Bi particles from aggregation and thus to ensure short K-ion diffusion for efficient K-ion uptake/release in each Bi nanoparticles.

On the other hand, benefiting from intimate contact between the Bi and the Co nanoparticles, Bi can effectively react with K-ions with the help of Co nanoparticles which act as conductive "binder" for ensuring efficient electron transport. Such enhanced potassiation/de-potassiation kinetics in these metastable materials can be reflected by electrochemical analysis. Figures 4(a)–4(c) show cyclic voltammetry (CV) curves of Bi@C, $Bi_{0.85}Co_{0.15}$@C, and $Bi_{0.83}Fe_{0.17}$@C electrodes after initial potassiation/de-potassiation. With increasing scan rates, the CV curve profiles of Bi@C electrode change with disappearance of potassiation peak (peak A in Fig. 4(a)) due to relative sluggish K-ion storage kinetics. In contrast, changes of CV profiles and shift of K-ion uptake/release peaks are negligible in $Bi_{0.85}Co_{0.15}$@C and $Bi_{0.83}Fe_{0.17}$@C electrodes (Figs. 4(b) and 4(c)). To better understand the differences of kinetics in the three electrodes, their apparent K-ion diffusion coefficients ($D_{K\text{-ion}}$) are determined from the well-observed de-potassiation peak (peak B) using the Randles–Sevcik equation [35, 36]

$$i = 2.69 \times 10^5 \times A \times n^{2/3} \times D_{K\text{-ion}}{}^{1/2} \times C_0 \times v^{1/2}$$

where, i, $D_{K\text{-ion}}$, and v stand for the peak current, the apparent K-ion diffusion coefficient, and the potential scan rate, respectively. A, n, and C_0 represent the effective surface area of the electrode, the number of electrons transferred in a unit reaction, and the concentration of the diffusion species, respectively. By plotting i vs. $v^{1/2}$ (insets of Figs. 4(a)–4(c)), the $D_{K\text{-ion}}$ of Bi@C, $Bi_{0.85}Co_{0.15}$@C, and $Bi_{0.83}Fe_{0.17}$@C electrodes are 7.9×10^{-11}, 3.1×10^{-10}, and 5.6×10^{-10} cm^2·s^{-1}, respectively. These again confirm that the alloy electrodes have much faster K-ion diffusion kinetics. The importance of inactive metallic precipitates is also shown from electrochemical impedance spectroscopy (EIS). Figures 4(d)–4(f) are EIS spectra of half PIBs employing Bi@C, $Bi_{0.85}Co_{0.15}$@C, and $Bi_{0.83}Fe_{0.17}$@C anodes respectively after different discharge/charge cycles. Upon cycling, the charge transfer resistance (diameter of the semicircle at low Z') of the Bi@C increases along with the cycling numbers, gradually increasing from approximately 15 to 60 Ω after 30 cycles (Fig. 4(d)). Interestingly, the situations are much improved after alloying with Co or Fe. In particular, the resistance of the $Bi_{0.83}Fe_{0.17}$@C anode is stabilized after 10 cycles (Fig. 4(f)).

Based on above results, the phase and morphology changes of metastable Bi:Co@C structure are illustrated in Fig. 4(g). The precipitated elemental Co nanoparticles play key roles as "binders" and "separators" to ensure fast and reversible K-ion storage in the precipitated Bi nanoparticles from Bi:Co metastable alloy. Even more attractive is that the performance enhancement is obtained with a significant cost reduction when expensive Bi (~ 10,300 USD/ton) is partially replaced with a much cheaper metal such as Fe (~ 93 USD/ton).

To further investigating application potential of the prepared alloy anodes, full PIBs with a polymer cathode (PTCDA-0C, a polymer with 3,4,9,10-perylene-tetracarboxylic acid-dianhydride and hydrazine), a pre-potassiated $Bi_{0.85}Co_{0.15}$@C anode, and a 1 M KPF_6/DME electrolyte were assembled. PTCDA-0C is an organic cathode with good rate capability, as demonstrated in our previous

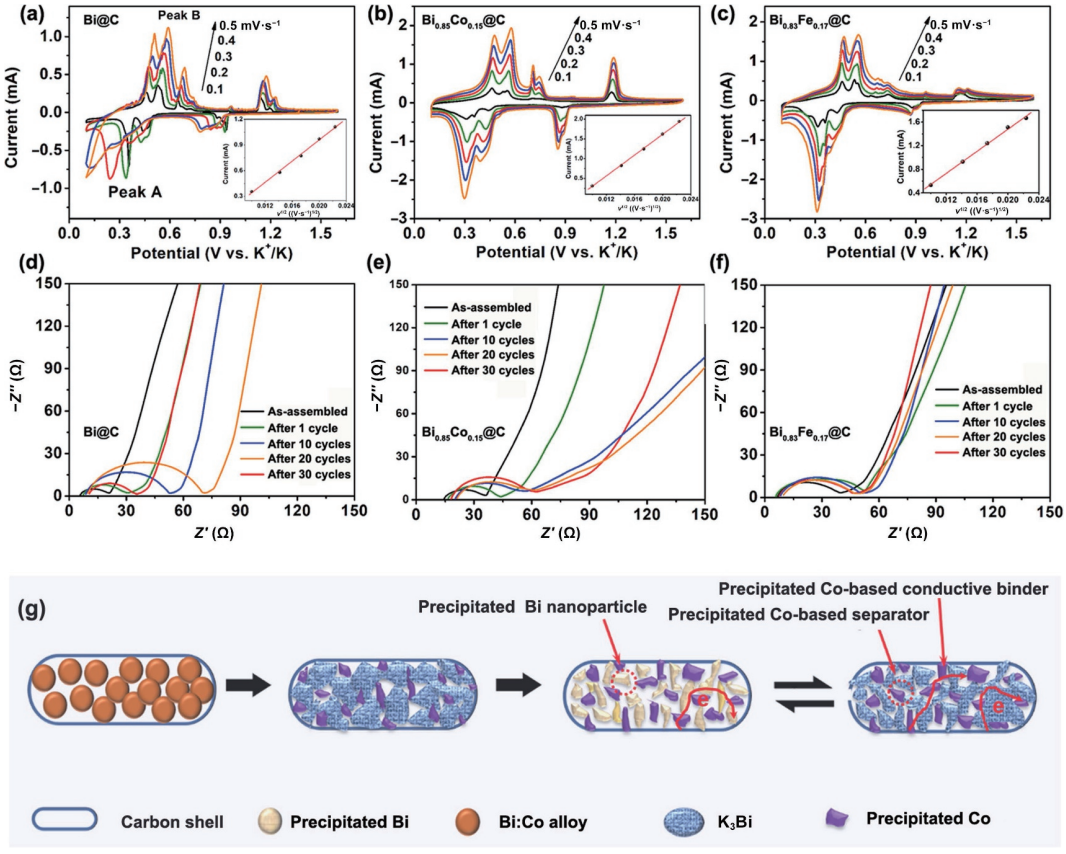

Figure 4 Electrochemical analysis of MOF-derived materials. CV curves of the Bi@C (a), the $Bi_{0.85}Co_{0.15}$@C (b), and the $Bi_{0.83}Fe_{0.17}$@C (c) electrodes under different sweep rates. Inset figures are *i* vs. $v^{1/2}$ plots. EIS spectra of the Bi@C (d), the $Bi_{0.85}Co_{0.15}$@C (e), and the $Bi_{0.83}Fe_{0.17}$@C (f) electrodes after different discharge/charge cycles. (g) Schematic diagram illustrating the phase and morphology changes of the metastable Bi:Co@C (b) structures during the discharge/charge processes.

works (Fig. S10 in the ESM) [37]. Typically, K-ions are inserted into the $Bi_{0.85}Co_{0.15}$@C anode and extracted from the PTCDA-0C cathode during charging in full battery, and *vice versa* during discharging (Fig. 5(a)).

The assembled full cell exhibits excellent electrochemical performance at various current densities (Figs. 5(b) and 5(c)). Specially, the full cell delivers reversible capacities of 107, 98, 91, and 84 mAh·g^{-1} at 0.1, 0.2, 0.5, and 1 A·g^{-1}, respectively. After cycling at high current density, the capacity of the full cell can be restored back to 94 mAh·g^{-1} when the current density is reduced back to 0.2 A·g^{-1}, demonstrating the superior capacity recoverability. The assembled full PIB can deliver both high

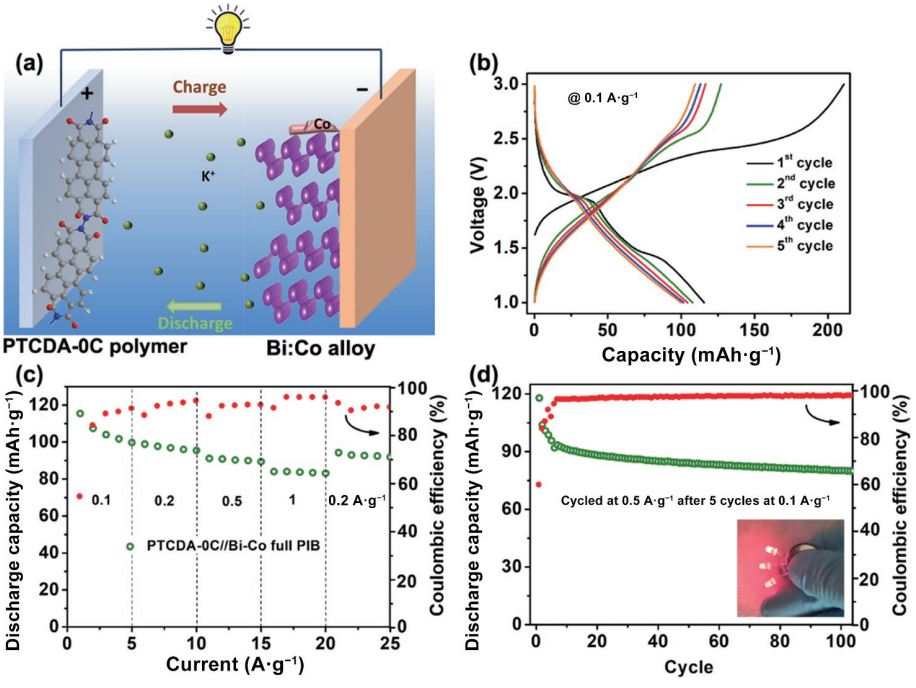

Figure 5 Electrochemical properties of full batteries with MOF-derived anode. (a) Schematic illustration of the PTCDA-0C//$Bi_{0.85}Co_{0.15}$@C PIB. (b) Initial discharge/charge curves of the assembled full PIB at 0.1 A·g^{-1}. (c) and (d) Rate capability and cycling performance of the assembled full PIB, respectively. The inset digital photo shows the power of the assembled full PIB.

energy and power densities (170.18 and 133.6 Wh·kg^{-1} at 167 and 1,670 W·kg^{-1}, respectively). The cycle stability of the full PIB is further investigated (Fig. 5(d)). After the first 5 cycles for activation at 0.1 A·g^{-1}, the assembled PIB exhibits good cycle stability over 100 cycles with a capacity retention of 86% (80 mAh·g^{-1}) at 0.5 A·g^{-1}.

3 Conclusions

In summary, we proposed and fabricated, for the first time, Bi:Fe and Bi:Co metastable alloy nanodots@carbon structures via a facile MOF-assistant annealing method. Comparing with the Bi@C electrode, the Bi:Co@C and the Bi:Fe@C electrodes demonstrate significantly improved mass loading-independent rate and cycling performance with high K-ion uptake/release kinetics. Under high current density of 20 A·g^{-1}, $Bi_{0.85}Co_{0.15}$@C and $Bi_{0.83}Fe_{0.17}$@C electrodes respectively deliver superior 178 and 253 mAh·g^{-1}, meanwhile only 77 mAh·g^{-1} is obtained in Bi@C electrode. *Ex situ* SEM, XPS, XRD, and TEM studies on the Bi:Co@C material indicate that inactive elemental Co nanoparticles separate out during the potassiation process, acting as efficient electron transport pathways, preventing the adjacent precipitated Bi nanoparticles from aggregation, and accelerating the potassiation/de-potassiation kinetics during the following cycles. The prepared Bi:Co and Bi:Fe alloy nanodots@carbon structures can be promising anode materials for PIBs. Furthermore, the proposed metastable alloy types and material synthesis method could provide new insights on the high-performance metal anodes for batteries.

Acknowledgements

This work was supported by the NSFC/RGC Joint Research Scheme 2020/21 (No. N_CityU104/20).

Electronic Supplementary Material: Supplementary material (experimental details including the material synthesis, characterizations, electrochemical measurements, and supplementary figures) is available in the online version of this article at https://doi.org/10.1007/s12274-022-4398-z.

References

[1] Zhao, S. Q.; Guo, Z. Q.; Yan, K.; Guo, X.; Wan, S. W.; He, F. R.; Sun, B.; Wang, G. X. The rise of Prussian blue analogs: Challenges and opportunities for high-performance cathode materials in potassium-ion batteries. *Small Struct.* **2021**, *2*, 2000054.

[2] Wang, H. G.; Wang, H. D.; Si, Z. J.; Li, Q.; Wu, Q.; Shao, Q.; Wu, L. L.; Liu, Y.; Wang, Y. H.; Song, S. et al. A bipolar and self-polymerized phthalocyanine complex for fast and tunable energy storage in dual-ion batteries. *Angew. Chem., Int. Ed.* **2019**, *131*, 10310–10314.

[3] Wang, H. G.; Wu, Q.; Wang, Y. H.; Wang, X.; Wu, L. L.; Song, S. Y.; Zhang, H. J. Molecular engineering of monodisperse SnO_2 nanocrystals anchored on doped graphene with high-performance lithium/sodium-storage properties in half/full cells. *Adv. Energy Mater.* **2019**, *9*, 1802993.

[4] Huang, H. W.; Wang, J. W.; Yang, X. F.; Hu, R. Z.; Liu, J. L.; Zhang, L.; Zhu, M. Unveiling the advances of nanostructure design for alloy-type potassium-ion battery anodes via *in situ* TEM. *Angew. Chem., Int. Ed.* **2020**, *132*, 14612–14618.

[5] Zhang, X. D.; Yue, F. S.; Liang, J. Y.; Shi, J. L.; Li, H.; Guo, Y. G. Structure design of cathode electrodes for solid-state batteries: Challenges and progress. *Small Struct.* **2020**, *1*, 2000042.

[6] Xu, D.; Chen, L.; Su, X. Z.; Jiang, H. L.; Lian, C.; Liu, H. L.; Chen, L.; Hu, Y. J.; Jiang, H.; Li, C. Z. Heterogeneous $MoSe_2$/nitrogen-doped-carbon nanoarrays: Engineering atomic interface for potassium-ion storage. *Adv. Funct. Mater.* **2022**, *32*, 2110223.

[7] Hu, C.; Ma, K.; Hu, Y. J.; Chen, A.; Saha, P.; Jiang, H.; Li, C. Z. Confining MoS_2 nanocrystals in MOF-derived carbon for high performance lithium and potassium storage. *Green Energy Environ.* **2021**, *6*, 75–82.

[8] Song, K. M.; Liu, C. T.; Mi, L. W.; Chou, S. L.; Chen, W. H.; Shen, C. Y. Recent progress on the alloy-based anode for sodium-ion batteries and potassium-ion batteries. *Small* **2021**, *17*, 1903194.

[9] Heligman, B. T.; Kreder, K. J.; Manthiram, A. Zn-Sn interdigitated eutectic alloy anodes with high volumetric capacity for lithium-ion batteries. *Joule* **2019**, *3*, 1051–1063.

[10] Chen, K. T.; Tuan, H. Y. Bi-Sb nanocrystals embedded in phosphorus as high-performance potassium ion battery electrodes. *ACS Nano* **2020**, *14*, 11648–11661.

[11] Wang, J.; Fan, L.; Liu, Z. M.; Chen, S. H.; Zhang, Q. F.; Wang, L. L.; Yang, H. G.; Yu, X. Z.; Lu, B. G. *In situ* alloying strategy for exceptional potassium ion batteries. *ACS Nano* **2019**, *13*, 3703–3713.

[12] Wang, S. H.; Yi, Z.; Wang, X. X.; Sun, Q. J.; Cheng, Y.; Wang, L. M. A rational design to buffer volume expansion of CoSn intermetallic in lithium and sodium storage: Multicore-shell versus monocore-shell. *Energy Storage Mater.* **2019**, *23*, 629–635.

[13] Gao, H.; Guo, X.; Wang, S. J.; Zhang, F.; Liu, H.; Wang, G. X. Antimony-based nanomaterials for high-performance potassium-ion batteries. *EcoMat* **2020**, *2*, e12027.

[14] Xu, J. Y.; Lai, C. L.; Duan, L. P.; Zhang, Y. X.; Xu, Y. F.; Bao, J. C.; Zhou, X. S. Anchoring ultrafine CoP and CoSb nanoparticles into rich N-doped carbon nanofibers for efficient potassium storage. *Sci. China Mater.* **2022**, *65*, 43–50.

[15] Imtiaz, S.; Amiinu, I. S.; Xu, Y.; Kennedy, T.; Blackman, C.; Ryan, K. M. Progress and perspectives on alloying-type anode materials for advanced potassium-ion batteries. *Mater. Today* **2021**, *48*, 241–269.

[16] Raabe, D.; Li, Z. M.; Ponge, D. Metastability alloy design. *MRS Bull.* **2019**, *44*, 266–272.

[17] Tan, H. T.; Chen, D.; Rui, X. H.; Yu, Y. Peering into alloy anodes for sodium-ion batteries: Current trends, challenges, and opportunities. *Adv. Funct. Mater.* **2019**, *29*, 1808745.

[18] Li, B.; Shang, S. L.; Zhao, J. W.; Itkis, D. M.; Jiao, X. X.; Zhang, C. F.; Liu, Z. K.; Song, J. X. Metastable trigonal SnP: A promising anode material for potassium-ion battery. *Carbon* **2020**, *168*, 468–474.

[19] Gabaudan, V.; Berthelot, R.; Stievano, L.; Monconduit, L. Inside the alloy mechanism of Sb and Bi electrodes for K-ion batteries. *J. Phys. Chem. C* **2018**, *122*, 18266–18273.

[20] Lei, K. X.; Wang, C. C.; Liu, L. J.; Luo, Y. W.; Mu, C. N.; Li, F. J.; Chen, J. A porous network of bismuth used as the anode material for high-energy-density potassium-ion batteries. *Angew. Chem., Int. Ed.* **2018**, *57*, 4687–4691.

[21] Jiao, T. P.; Wu, S. L.; Cheng, J. Y.; Chen, D.; Shen, D.; Wang, H.; Tong, Z. Q.; Li, H.; Liu, B.; Kai, J. J. et al. Bismuth nanorod networks confined in a robust carbon matrix as long-cycling and high-rate potassium-ion battery anodes. *J. Mater. Chem. A* **2020**, *8*, 8440–8446.

[22] Yang, H.; Xu, R.; Yao, Y.; Ye, S. F.; Zhou, X. F.; Yu, Y. Multicore-shell Bi@N-doped carbon nanospheres for high power density and long cycle life sodium-and potassium-ion anodes. *Adv. Funct. Mater.* **2019**, *29*, 1809195.

[23] Sun, X. P.; Zhang, B.; Chen, M.; Wang, L.; Wang, D. B.; Man, R. X.; Iqbal, S.; Tian, F.; Qian, Y. T.; Xu, L. Q. Space-confined growth of Bi_2Se_3 nanosheets encapsulated in N-doped carbon shell lollipop-like composite for full/half potassium-ion and lithium-ion batteries. *Nano Today* **2022**, *43*, 101408.

[24] Tong, Z. Q.; Yang, R.; Wu, S. L.; Shen, D.; Jiao, T. P.; Zhang, K. L.; Zhang, W. J.; Lee, C. S. Defect-engineered vanadium trioxide nanofiber bundle@graphene hybrids for high-performance all-vanadate Na-ion and K-ion full batteries. *J. Mater. Chem. A* **2019**, *7*, 19581–19588.

[25] Su, S. L.; Liu, Q.; Wang, J.; Fan, L.; Ma, R. F.; Chen, S. H.; Han, X.; Lu, B. G. Control of SEI formation for stable potassium-ion battery anodes by Bi-MOF-derived nanocomposites. *ACS Appl. Mater. Interfaces* **2019**, *11*, 22474–22480.

[26] Cheng, X. L.; Li, D. J.; Wu, Y.; Xu, R.; Yu, Y. Bismuth nanospheres

embedded in three-dimensional (3D) porous graphene frameworks as high performance anodes for sodium- and potassium-ion batteries. *J. Mater. Chem. A* **2019**, *7*, 4913–4921.

[27] Zhang, R. D.; Bao, J. Z.; Wang, Y. H.; Sun, C. F. Concentrated electrolytes stabilize bismuth-potassium batteries. *Chem. Sci.* **2018**, *9*, 6193–6198.

[28] Zhang, W. C.; Mao, J. F.; Li, S. A.; Chen, Z. X.; Guo, Z. P. Phosphorus-based alloy materials for advanced potassium-ion battery anode. *J. Am. Chem. Soc.* **2017**, *139*, 3316–3319.

[29] Wang, H.; Wu, X.; Qi, X. J.; Zhao, W.; Ju, Z. C. Sb nanoparticles encapsulated in 3D porous carbon as anode material for lithium-ion and potassium-ion batteries. *Mater. Res. Bull.* **2018**, *103*, 32–37.

[30] Zhang, W. C.; Pang, W. K.; Sencadas, V.; Guo, Z. P. Understanding high-energy-density Sn_4P_3 anodes for potassium-ion batteries. *Joule* **2018**, *2*, 1534–1547.

[31] Wang, L. P.; Yang, J. Y.; Li, J.; Chen, T.; Chen, S. L.; Wu, Z. R.; Qiu, J. L.; Wang, B. J.; Gao, P.; Niu X. et al. Graphite as a potassium ion battery anode in carbonate-based electrolyte and ether-based electrolyte. *J. Power Sources* **2019**, *409*, 24–30.

[32] Wang, W.; Zhou, J. H.; Wang, Z. P.; Zhao, L. Y.; Li, P. H.; Yang, Y.; Yang, C.; Huang H. X.; Guo, S. J. Short-range order in mesoporous carbon boosts potassium-ion battery performance. *Adv. Energy Mater.* **2018**, *8*, 1701648.

[33] Tong, Z. Q.; Yang, R.; Wu, S. L.; Shen, D.; Jiao, T. P.; Zhang, K. L.; Zhang, W. J.; Lee, C. S. Surface-engineered black niobium Oxide@Graphene nanosheets for high-performance sodium-/potassium-ion full batteries. *Small* **2019**, *15*, 1901272.

[34] Wang, X.; Qian, K.; Chen, X. Y.; Sun, X. L.; Guo, C.; Li, J. F. *In situ* perfusing Sb particles into porous N-doped carbon microspheres and their electrochemical properties in potassium ion batteries. *J. Alloys Compd.* **2022**, *906*, 164263.

[35] Tong, Z. Q.; Kang, T. X.; Wan, Y. P.; Yang, R.; Wu, Y.; Shen, D.; Liu, S. H.; Tang, Y. B.; Lee, C. S. A Ca-ion electrochromic battery via a water-in-salt electrolyte. *Adv. Funct. Mater.* **2021**, *31*, 2104639.

[36] Tong, Z. Q.; Hao, J.; Zhang, K.; Zhao, J. P.; Su, B. L.; Li, Y. Improved electrochromic performance and lithium diffusion coefficient in three-dimensionally ordered macroporous V_2O_5 films. *J. Mater. Chem. C* **2014**, *2*, 3651–3658.

[37] Tong, Z. Q.; Tian, S.; Wang, H.; Shen, D.; Yang R.; Lee, C. S. Tailored redox kinetics, electronic structures and electrode/electrolyte interfaces for fast and high energy-density potassium-organic battery. *Adv. Funct. Mater.* **2020**, *30*, 1907656.